Long-working-distance incoherent-light interference microscope

Michael B. Sinclair, Maarten P. de Boer, and Alex D. Corwin

We describe the design and operation of a long-working-distance, incoherent light interference microscope that has been developed to address the growing demand for new microsystem characterization tools. The design of the new microscope is similar to that of a Linnik interference microscope and thus preserves the full working distance of the long-working-distance objectives utilized. However, in contrast to a traditional Linnik microscope, the new microscope does not rely on the use of matched objectives in the sample and the reference arms of the interferometer. An adjustable optical configuration has been devised that allows the total optical path length, wavefront curvature, and dispersion of the reference arm to be matched to the sample arm of the interferometer. The reference arm configuration can be adjusted to provide matching for 5×, 10×, and 20× long-working-distance objectives in the sample arm. In addition to retaining the full working distance of the sample arm objectives, the new design allows interference images to be acquired in situations in which intervening windows are necessary, such as occur with packaged microsystems, microfluidic devices, and cryogenic, vacuum, or environmental chamber studies of microsystem performance. The interference microscope is compatible with phase-shifting interferometry, vertical scanning interferometry, and stroboscopic measurement of dynamic processes. © 2005 Optical Society of America

OCIS codes: 120.3180, 180.3170.

1. Introduction

Over the past few years, increasing emphasis has been placed on the development of miniaturized mechanical, electromechanical, optomechanical, and microfluidic systems. These microsystems can offer significant advantages over traditional systems, such as small form factors, highly robust construction, low power consumption, and manufacture by precise, high-volume microlithographic processes developed initially for the semiconductor industry. As a consequence, the demand for new tools and instruments capable of characterizing the fabrication and performance of microsystems has also increased. Interference microscopy has received considerable attention in this regard, since it provides accurate, noncontact measurement of the out-of-plane motion of microfabricated components.[1–4] As such, it can be used to measure the performance of moving components, as well as distortions of structures that are due to stress relaxation.

The authors are with Sandia National Laboratories, Albuquerque, New Mexico 87185.

When coupled with appropriate test structures and numerical analysis, interference microscopy can also be used for the determination of material properties such as Young's modulus, stress gradients and beam takeoff angles,[5] residual stress levels,[6] adhesion,[7,8] and adhesion hysteresis.[9] However, for a variety of reasons, it is often difficult to apply traditional interference microscopy to microsystem characterization. As described below, traditional interference objectives are characterized by relatively short working distances. This complicates their use in cases in which it is necessary to place components such as actuating electrical probes or probe cards between the device under test and the objective. In addition, there are many instances in which one wishes to perform interference measurements on devices in windowed packages or located in cryogenic, vacuum, or environmental chambers. Here, the short working distance, combined with the difficulty associated with compensating for the window, prevents the use of traditional interference objectives. Thus the development of new configurations for interference microscopy, tailored to the needs of microsystem characterization, is of interest.

The field of interference microscopy is relatively mature, and many different microscope designs have been developed to address wide-ranging applications. Designs appearing in the literature span the range from

point-scanning instruments[10–12] to whole-field imaging systems[13–20] and from laser-illuminated instruments[4,10,12] to incoherently illuminated systems.[3,13–20] The present work is devoted to an incoherently illuminated, whole-field imaging interference microscope. Incoherent illumination was selected to avoid difficulties associated with coherent light imaging and to take advantage of the excellent image quality provided by incoherent light illumination. In addition, the finite fringe envelope obtained with incoherent illumination allows vertical scanning interferometry (VSI) techniques to be utilized to determine the magnitude of step discontinuities.

Incoherent light interference microscopes must achieve precise optical-path-length matching between the sample and the reference arms of the interferometer because of the short coherence length associated with incoherent illumination. Such microscopes can be loosely categorized into two main groups: microscopes utilizing interference objectives and Linnik-type microscopes.[13,14] Interference objectives, such as Mirau and Michelson objectives,[15,18] are relatively inexpensive, easy to use, and, for appropriate specimens, produce excellent interferograms. With such objectives, the interferometer is arranged in the space between the final optical element of the objective and the specimen. This leads to two distinct advantages. First, the optical path length of each arm of the interferometer is small (~5–10 mm), enhancing the stability of the interference images. Second, since the interferometer is located after the image-forming optics, few components are needed, and it is easy to match the optical characteristics (such as wavefront and dispersion) of the two arms. The primary drawback of these interference objectives is lack of working distance—the interferometer optics located between the objective and the specimen utilizes the majority of the objective's working distance, leaving only a small working distance between the objective housing and the specimen. A second disadvantage of conventional interference objectives is their inability to produce interferograms when a window is positioned between the objective and the sample under investigation. Although, in principle, a matched window could be placed in the reference arm of the interferometer, in practice this is difficult to achieve and usually requires some disassembly of the objective.

The Linnik interference microscope[13,14] overcomes the shortcomings of the interference objective by positioning the two arms of the interferometer around the primary beam splitter of the microscope. Nominally identical objectives are used in both arms to ensure a high degree of optical matching. In this way, the full working distance of the objective is retained. In addition, the Linnik approach is more amenable to the inclusion of windows on both the sample and the reference arms of the interferometer. A significant disadvantage of the Linnik approach is the expense associated with the purchase of an additional objective for each desired magnification and the degree to which the sample and the reference objectives must be matched. Typical manufacturing tolerances do not ensure that any two "identical" objectives are sufficiently well matched. Rather, matched pairs must be selected from a pool of "identical" objectives. Thus, obtaining such a pair of matched objectives can entail considerable expense. In addition, one must repeat the selection process for each desired magnification.

In this paper, we describe the design and operation of a long-working-distance incoherent light interference microscope that has been developed to address the growing demand for new microsystem characterization tools. The design of the new microscope is most similar to that of a Linnik interference microscope and thus preserves the full working distance of the long-working-distance objectives utilized. However, in contrast to a traditional Linnik microscope, the new microscope does not rely on the use of matched objectives in the sample and the reference arms of the interferometer. An adjustable optical configuration has been devised that allows the total optical path length, wavefront curvature, and dispersion of the reference arm to be matched to the sample arm of the interferometer. The reference arm configuration can be adjusted to provide matching for $5\times$, $10\times$, and $20\times$ long-working-distance objectives in the sample arm. In addition to retaining the full working distance of the sample arm objectives, the new design allows interference images to be acquired in situations in which intervening windows are necessary, such as occur with packaged microsystems, microfluidic devices, or when the device of interest is located in a cryogenic, vacuum, or environmental chamber.

2. Microscope Design

To produce high-quality interferograms by use of incoherent illumination, an interference microscope must satisfy four criteria. First, it is obvious that the sample and the reference objectives must be accurately focused on the specimen and reference surface, respectively. The second criterion is that the overall group delay experienced by a wave packet traversing the sample arm of the interferometer be equal to the group delay of the reference arm. A wave packet incident upon the interferometer will be divided into two identical copies by the beam splitter. The two copies traverse the two arms of the interferometer and are recombined at the beam splitter. Coherent recombination will occur only if both wave packets arrive at the beam splitter within a time interval given by the coherence time of the illumination source. The third criterion for the production of high-quality interferograms is that the total group-velocity dispersion present in the two arms of the interferometer be matched. For a perfectly balanced interferometer, identical amounts of dispersion occur in each arm, and the net phase difference between the two arms is constant across the bandwidth of the illumination source. Fringe visibility is decreased for an imbalanced interferometer, as the phase difference will now vary with wavelength and it is no longer possible to achieve perfect constructive or destructive interference across the bandwidth of the source. The
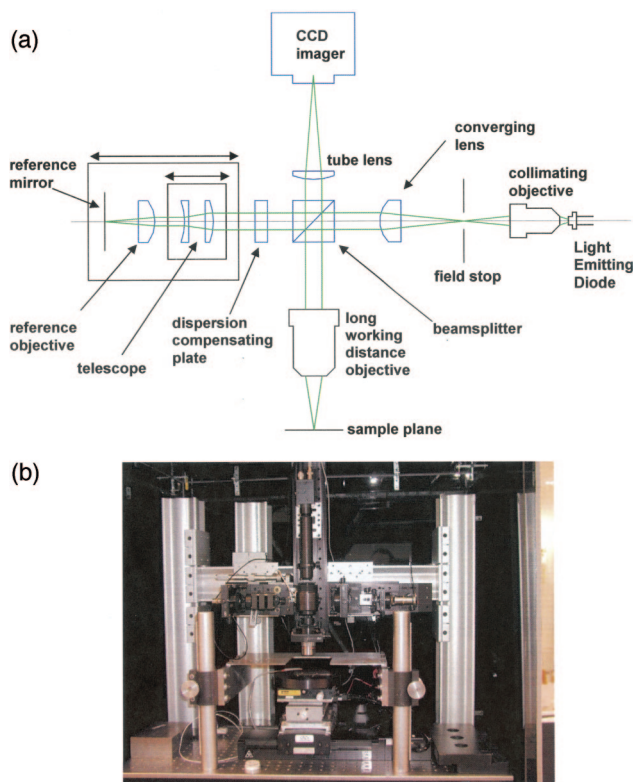
(a)

(b)

Fig. 1. (a) Schematic layout of the interference microscope. The microscope is constructed primarily from commercial optics and optomechanics. (b) Photograph of the interferometer coupled to a computer-controlled probe station for wafer-level measurement of microelectromechanical-system material parameters.

fourth criterion is that the positions of the back focal planes of the objectives in the two arms of the interferometer be equidistant from the beam splitter. This will ensure that the curvatures of the coherently recombining wavefronts are identical and that flat interference fringes are obtained. If this condition is not fulfilled, the interference fringes will exhibit a characteristic "bull's-eye" pattern.

A schematic of the optical layout of the interferometer is shown in Fig. 1(a), and Fig. 1(b) shows a photograph of the interferometer coupled with a computerized probe station for wafer-level testing of material properties. The interference microscope is constructed primarily from commercially available optics and optomechanics. The illumination source is a green light-emitting diode (LED). Green LED illumination was chosen for its relative brightness, its compatibility with high-bandwidth modulation that is required for stroboscopic measurements, and because the green wavelengths are strongly absorbed by polycrystalline silicon (polysilicon), thereby eliminating potential artifacts. The emission from this diode peaks at 525 nm, and the full width at half-maximum of the emission spectrum is approximately 40 nm. For use in the interferometer, the LED is embedded in an aluminum disk and the front lens of the LED is lapped and polished, resulting in a flat front face of the LED package located less than 1 mm from the

emitting element. The emitting element is positioned in the front focal plane of an infinity-corrected $10\times$ microscope objective, and a field iris is located immediately after the objective. The field iris is, in turn, located in the front focal plane of a converging lens (88.9-mm focal length), which relays the image of the source onto the back focal planes of the sample and the reference objectives. Note that the illumination system slightly underfills the pupils of the reference and sample objectives to ensure equal throughout for both objectives. The beam splitter utilized is a broadband, nonpolarizing, cube-type beam splitter. The sample arm of the interferometer contains an infinity-corrected long-working-distance Mitutoyo M Plan Apo objective. The microscope is optimized to accept objectives with three different magnifications: a $5\times$, NA 0.14, objective with a 34-mm working distance, a $10\times$, NA 0.28, objective with a 33.5-mm working distance, and a $20\times$, NA 0.42, objective with a 20.0-mm working distance. The sample under investigation is positioned at the front focal plane of this objective. Thus the sample plane is conjugate with the plane of the field iris. The radiation reflected from the sample returns through the objective, passes through the beam splitter, and is focused at the plane of a CCD camera by means of a 200-mm focal-length tube lens.

The reference arm of the interferometer is more complex than the sample arm because it contains the adjustable components required to allow matching of different sample arm objectives. The reference objective is an achromatic doublet (31.0-mm focal length), and the reference mirror is positioned at its front focal plane, which is also conjugate with the field stop. The reference mirror is mounted on a piezoelectric actuator to facilitate phase-shifting interferometry (PSI). Two types of mirrors are employed: a first surface metal mirror for use with highly reflective samples or a silicon mirror to optimize fringe contrast when the interferometer is to be used on polysilicon Microelectromechanical systems (MEMS). To facilitate matching of the optical path lengths, the entire reference arm assembly is constructed on a linear translation stage. However, because different optical components are used in the two arms of the interferometer, the position of the stage that matches path lengths will not simultaneously match the positions of the back focal planes of the arms. As a result, the curvatures of the coherently combining wavefronts from the sample and the reference arms will differ and a bull's-eye fringe pattern will be produced. To remedy this, a low-power afocal Galilean telescope (constructed from a 50.8-mm focal-length positive achromat and a 35.0-mm focal-length negative achromat) is inserted between the reference objective and the beam splitter. The telescope is mounted on a translation stage that is in turn mounted on the translation stage responsible for path-length matching. One can adjust the location of the back focal plane by moving the telescope along the optical axis of the reference arm. This ensures that straight fringes can be obtained. Note that, because the tele-
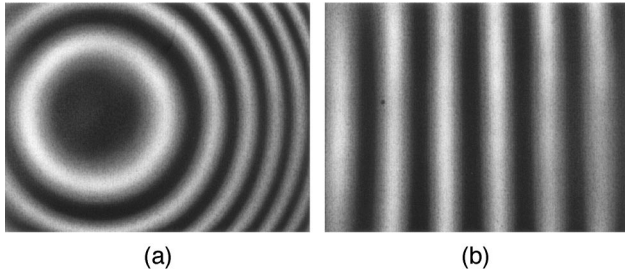
Fig. 2. (a) Interference fringes obtained when the telescope is adjusted so that the back focal planes of the sample and the reference arms are not equidistant from the beam splitter; (b) after adjustment of the telescope straight fringes are obtained. The sample was slightly tilted when these interferograms were obtained.
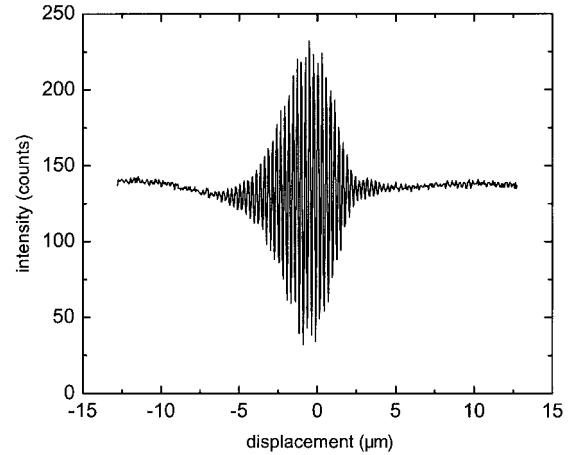

Fig. 3. Representative interferogram obtained with a 6.4-mm-thick fused silica compensating plate. For this compensator a fringe contrast of approximately 0.7 is obtained.

scope is afocal, it can be moved without affecting the focus of the reference objective. In addition, the telescope can be moved without affecting the path-length matching. Figure 2 shows the appearance of the interference fringes for two positions of the telescope. Radiation reflected by the reference mirror returns through the objective, telescope, and beam splitter and is focused onto the CCD imager by the tube lens.

The final component in the reference arm is a plane-parallel compensation plate. A separate compensation plate is required for each type of objective. The thickness and glass type of the compensation plate must be carefully chosen to balance the interferometer. This can be done in a systematic manner as follows. First, note that the optical phase difference ϕ between the two arms of the interferometer is given by[19]

$$\phi = kZ(k), \tag{1}$$

where, because of dispersion, the optical path difference Z is, in general, a function of wave vector k. Expanding the optical phase difference in a Taylor series about the central wave vector k_0 (k_0 corresponds to the peak of the emission spectrum of the illumination source) yields[19]

$$\phi = k_0 Z(k_0) + \frac{d\phi}{dk}\bigg|_{k_0} (k - k_0)$$
$$+ \frac{1}{2} \frac{d^2\phi}{dk^2}\bigg|_{k_0} (k - k_0)^2 + \cdots +, \tag{2}$$

where the first term is the phase-velocity optical phase difference, the second term is the group-velocity optical phase difference, and the third and higher terms arise as a result of group-velocity dispersion. In practice, the first two terms in this expression will contain the desired surface topography information,[19] whereas the third term will result in broadening of the fringe envelope along with a decrease of fringe contrast. To select the optimal compensation plate, a mirror identical to the reference mirror placed at the sample plane and a series of

single-pixel interferograms (i.e., intensity versus vertical sample position for a single pixel) are obtained with compensation plates of differing thicknesses. The interferograms are Fourier transformed, and the phase in the neighborhood of k_0 is fit to a quadratic polynomial in the wave vector $(k - k_0)$. The second-order coefficient provides a measure of the amount of dispersion mismatch and will become zero for the optimal compensation plate thickness.

An example of the application of this procedure to find the optimal compensation plate thickness for the $10\times$ objective is shown in Figs. 3 and 4. A front surface metal mirror was mounted on a piezoelectric translation stage and placed at the sample plane. Compensating plates of four different thicknesses (0, 3.2, 6.4, and 9.6 mm) of fused silica were used in the reference arm. For each compensating plate, a 512-point interferogram was obtained with the sample mirror translated 0.05 μm between points. Figure 3 shows a representative single-pixel interferogram obtained with the 6.4-mm-thick plate. The phase profiles obtained by a Fourier transform of these interferograms are shown in Fig. 4(a). Also shown in Fig. 4(a) are the results of fitting a second-order polynomial to each of the phase profiles. The fitted region was restricted to the region about k_0 where the phase and magnitude of the Fourier transform exhibit a good signal-to-noise ratio. It is clear from Fig. 4(a) that the curvature of the phase profile decreases, changes sign, and then increases as the thickness of the compensator varies from 0 to 9.6 mm. Figure 4(b) shows a plot of the coefficient of the second-order term of the polynomial fit as a function of the thickness of the compensator plate. As expected, a linear dependence of the curvature on the thickness is observed. The measured slope of -5.9×10^6 compares favorably with a slope of -6.0×10^6 that is calculated from the wavelength dependence of the refractive index of fused silica. The thickness of the optimal compensator plate can be immediately determined from the zero crossing of the data of Fig. 4(b). The inter-
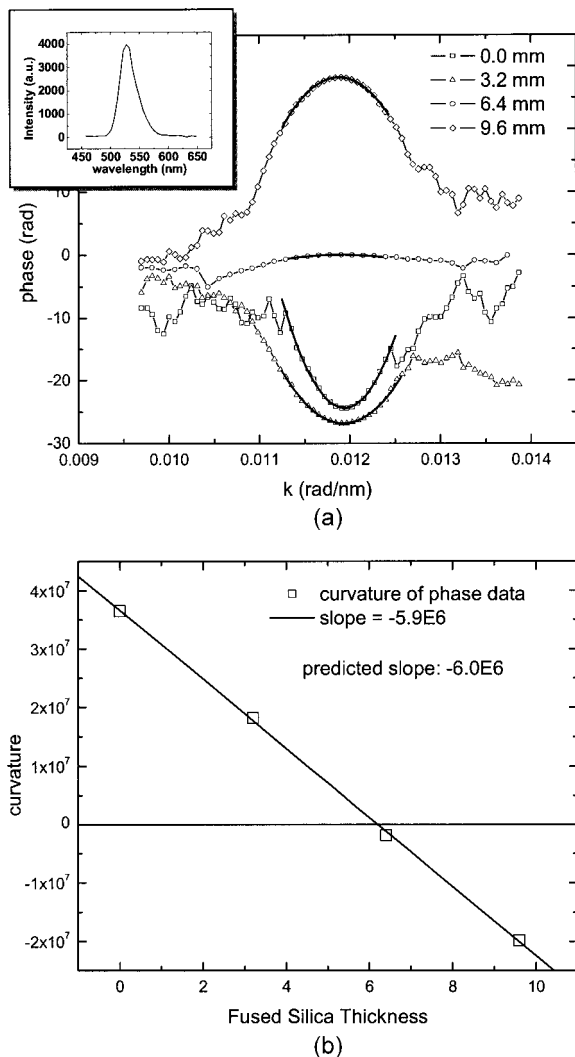
Fig. 4. (a) Graph of the phase of the Fourier transforms of inter-ferograms obtained for four different thicknesses of fused silica. The results of a quadratic fit to the phase profile are also shown. The inset shows the magnitude of the Fourier transform of one of the interferograms. (b) Graph of the coefficient of the second-order term of the quadratic fit as a function of fused silica thickness. The zero crossing of this line locates the optimal thickness of the compensation plate.

ferogram shown in Fig. 3 was thus obtained with a near-optimal compensator and, as a result, is narrow and exhibits good fringe contrast (~0.7). This procedure has also been applied to determine the optimal compensator plates for other objectives. It is important to note that, once an optimal compensator plate has been determined for a given objective power, other objectives of the same model are well compensated for dispersion.

The procedure outlined above eliminates only the leading term of the dispersion mismatch. This is justified in the current case because of the relatively narrow bandwidth of the illumination source. For broader sources (e.g., 200 nm), multiple compensation plates of different glass types can be utilized to eliminate successively higher-order dispersion terms.

A procedure of this sort has been presented in the context of stellar interferometry.[21,22] Also, in the case of broader sources, a different set of compensation plates might be required for different objectives of the same model type from the same manufacturer because of manufacturing tolerances.

Once the optimal compensator plate has been determined for each sample arm objective, sample arm objectives may be changed as follows. First the objective is changed, and the appropriate compensator plate is inserted. Then, the path-length-matching translation stage is adjusted to obtain high-contrast fringes. Finally, the telescope stage is adjusted to spread out the bull's-eye fringe pattern. In practice, the micrometer setting of each of the translation stages has been previously recorded, so that resetting the stages after the objective has been changed is fast and simple. One implementation of the interference microscope includes a five-position nosepiece for quick interchange of objectives.

3. Results

As a first test of the performance of the interference microscope, a step-height calibration standard was mounted on a piezoelectric actuated translation stage, and its surface profile was measured by use of VSI techniques.[17,19] A sequence of 512 interferometric image frames were obtained with the piezoelectric stage translated 0.05 μm along the optical axis between frames. In this manner a separate interferogram was obtained for each pixel in the field of view. By use of a procedure similar to that outlined in Ref. 19, each of these interferograms was Fourier transformed and the slope of each of the phase profiles was determined. The phase slope recorded for an x–y location within the frame is related to the height of surface at that location through

$$h(x, y) = \frac{1}{2} \left. \frac{d\phi}{dk} \right|_{k_0}. \tag{3}$$

Figure 5 shows the recovered surface profile, along with a line section along the surface. The measured step height of 10.20 μm is in good agreement with the quoted height of 10.14 ± 0.09 μm and confirms the accuracy of the interferometer. Further refinement of the surface profile can be obtained with the first term of Eq. (2).[19,23,24] However, when a simple version of this procedure is performed, "ghost steps" appear that are similar to those observed in Refs. 23 and 24. In this case, more sophisticated algorithms must be applied[23,24] to obtain the refined surface profile.

As an example of microsystem characterization, the surface profile of a polysilicon MEMS structure fabricated with Sandia National Laboratories SUMMIT V process[25] was obtained by use of VSI techniques. Briefly, the SUMMIT V™ micromachining process produces microstructures comprising five independent polysilicon structural levels. The MEMS structure used consists of several "pop-up" structures, one of which was partially actuated. Once

Fig. 6. One of the interferometric images in the sequence used to determine the surface profile of the MEMS device. Tight fringes appear on the structure to the right of center, indicating that it is substantially tilted. Broader fringes are observed on the structure to the left of center, which exhibits much less tilt.
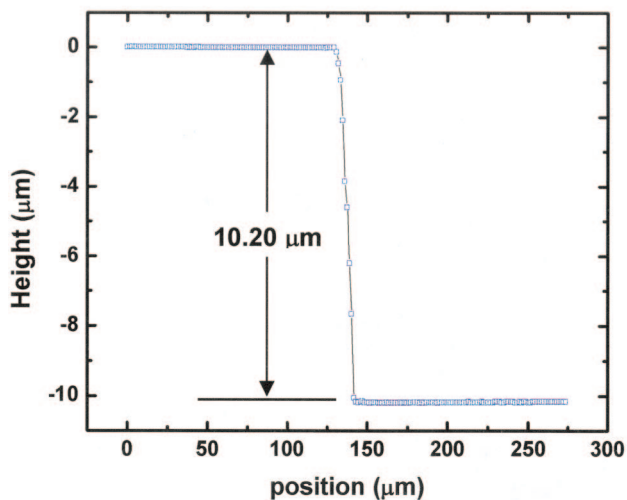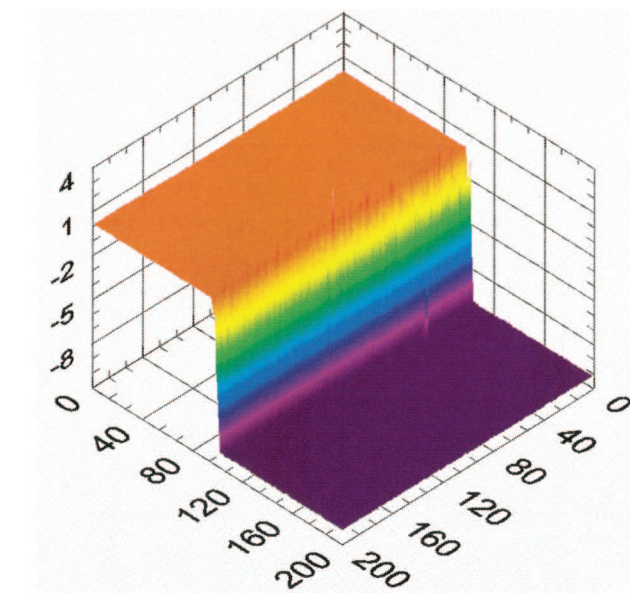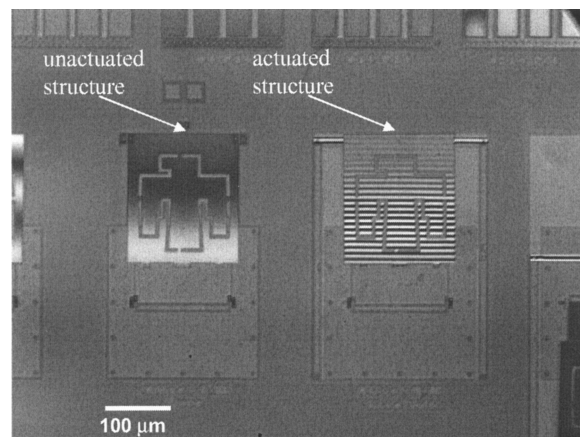

Fig. 5. Results of the surface reconstruction of the step-height standard: (a) portion of the reconstructed surface, (b) line scan across the step. The measured step height of 10.20 μm is in excellent agreement with the quoted height of 10.14 ± 0.09 μm.

again, a sequence of 512 frames was recorded at 0.05-μm intervals, and the phase-slope procedure described above was used to recover the surface profile. Figure 6 shows one interferogram of the sequence, obtained when the fringe envelope was partway up the tilted structure to the right of center. Fringes are also visible on the structure immediately to the left of the tilted structure. However, because this structure has not been actuated the fringes are relatively broad. Figure 7 shows a gray-scale image of the surface profile obtained with this procedure. As expected, a significant contrast gradient is visible on the actuated structure to the right of center, whereas little contrast variation is observed for the unactuated structure. Horizontal and vertical line scans of

the surface profile were recorded at the positions indicated by the red lines in Fig. 7. The vertical line scan shows that the actuated structure is tilting up by approximately 5 μm. The horizontal line scan shows that the surface height of the underlying polysilicon layer is successfully measured in the narrow gaps of the uppermost polysilicon layer. The step-height differences recorded between the different polysilicon levels are in close agreement with the known step heights of the SUMMIT V process.

Another example of the application of the interference microscope involves the use of PSI techniques[26,27] to accurately measure the curvature of micromachined polysilicon beams. Measurements of this type, when combined with appropriately designed test structures and analysis routines, can be
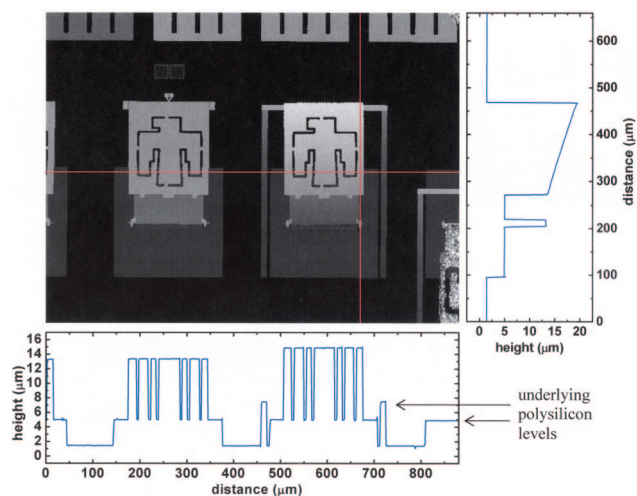

Fig. 7. Gray-scale image of the surface profile of the MEMS structure. A significant contrast gradient is observed on the pop-up structure to the right of center, indicating that this structure is substantially tilted. Horizontal and vertical line scans obtained at the locations of the red lines on the figure are also shown.
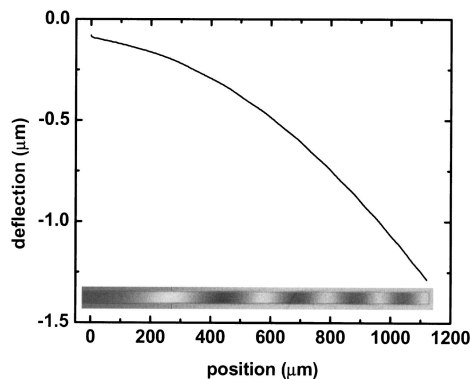
Fig. 8. Deflection of a polysilicon cantilever beam that is due to residual stress gradients. The inset shows one of the interferograms used with the PSI algorithm to obtain the beam deflection.

used to determine important material parameters such as residual stress level and stress gradient. Figure 8 shows an interferometric image of a polysilicon cantilever beam. Using the PSI approach, we obtained five such interferometric frames at $\pi/4$ phase shift intervals by moving the reference mirror piezoactuator. The surface profile of the continuous surface was then reconstructed with the Hariharan PSI algorithm.[27] The graph in Fig. 8 shows the recovered shape of the cantilever beam after a linear fit has been performed to remove any residual substrate tilt. A downward deflection of approximately 1.3 μm is observed that is due to polysilicon stress gradients.

As a final example of the utility of the new interference microscope, the ability of the microscope to record high-quality fringes in the case in which a window is placed between the objective and the sample is demonstrated. There are many cases in which the use of a window is necessary, including characterization of packaged optical MEMS parts, microfluidic devices, and testing of microsystems within environmental chambers or at cryogenic temperatures. Figure 9 shows two interferograms of a MEMS
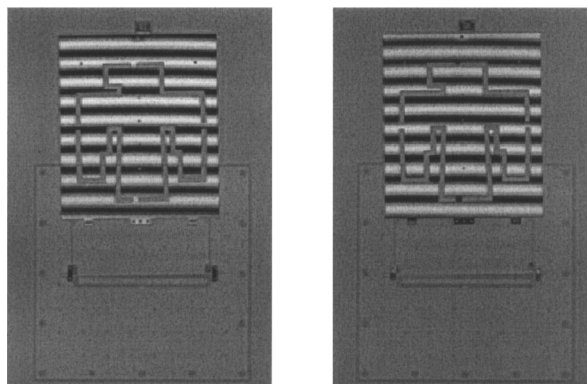

Fig. 9. Virtually identical interference images of a MEMS structure with no intervening window (left), and with a 1.6-mm window inserted between the objective and the sample (right). To compensate for the window, a corresponding plate was placed in the collimated region of the reference arm, and the path-length-matching translation stage was adjusted to obtain high-contrast fringes.

part. The interferogram shown on the left was taken without a window, and the interferogram on the right was obtained with a 1.6-mm-thick fused silica plate placed between the sample and the objective. To compensate for the window, a corresponding plate was placed in the collimated region of the reference arm, and the path-length-matching translation stage was adjusted to obtain high-contrast fringes. Note that, although fringes can be obtained with an intervening window, the optical aberrations induced by the addition of the window are not corrected. However, for relatively thin windows and low-magnification objectives this is not a significant problem.

4. Conclusions

The design of a new interference microscope, specifically optimized for the characterization of microsystems, has been described. The new microscope possesses a large working distance to allow room for components such as actuating electrical probes or probe cards between the device under test and the microscope objective. In addition, the microscope allows interferograms to be obtained in the case in which windows are required between the objective and the specimen. The microscope is compatible with VSI, PSI, and stroboscopic modes of data acquisition. A key feature of the new interference microscope is an adjustable reference arm optical assembly that allows three different sample side objectives to be used. The reference arm can be adjusted to simultaneously match optical path length, wavefront curvature, and group-velocity dispersion. A systematic method for selecting the compensating plate has been described.

As of this writing, seven copies of this design have been constructed and are being evaluated as tools for microsystem characterization at Sandia National Laboratories. These instruments have been used to study the behavior and reliability of microsystems in windowed environmental chambers and at cryogenic temperatures. In addition, one of these instruments has been integrated with an automated wafer-handling probe station to perform wafer-level testing of material properties obtained with Sandia's SUMMIT V surface micromachining process.

References

1. A. Bosseboeuf and S. Petitgrand, "Application of microscopic interferometry techniques in the MEMS field," in *Microsystems Engineering: Metrology and Inspection III,* C. Gorecki, ed., Proc. SPIE **5145,** 1–16 (2003).
2. A. Bosseboeuf and S. Petitgrand, "Characterization of the

static and dynamic behavior of M(O)EMS by optical techniques: Status and trends," J. Micromech. Microeng. **13,** S23–S33 (2003).

3. W. Hemmert, M. S. Mermelstein, and D. M. Freeman, "Nanometer resolution of three-dimensional motions using video interference microscopy," in *Proceedings of the 12th IEEE International Conference on Micro Electro Mechanical Systems* (Institute of Electrical and Electronics Engineers, 1999), pp. 302–308.

4. M. R. Hart, R. A. Conant, K. Y. Lau, and R. S. Muller, "Stroboscopic interferometer system for dynamic MEMS characterization," J. Microelectromech. Syst. **9,** 409–418 (2000).

5. B. D. Jensen, M. P. de Boer, and S. L. Miller, "IMaP: Interferometry for materials property evaluation in MEMS," in *International Conference on Modeling and Simulation of Microsystems, Semiconductors, Sensors and Actuators* (Computational Publications, 1999), pp. 206–209.

6. M. S. Baker, M. P. de Boer, N. F. Smith, L. K. Warne, and M. B. Sinclair, "Integrated measurement-modeling approaches for evaluating residual stress using micromachined fixed-fixed beams," J. Microelectromech. Syst. **11,** 743–753 (2002).

7. M. P. de Boer and T. A. Michalske, "Accurate method for determining adhesion of cantilever beams," J. Appl. Phys. **86,** 817–827 (1999).

8. J. A. Knapp and M. P. de Boer, "Mechanics of microcantilever beams subject to combined electrostatic and adhesive forces," J. Microelectromech. Syst. **11,** 754–764 (2002).

9. M. P. de Boer, J. A. Knapp, T. A. Michalske, U. Srinivasan, and R. Maboudian, "Adhesion hysteresis of silane coated microcantilevers," Acta Mater. **48,** 4531–4541 (2000).

10. Y. Bessho, "Surface roughness measuring apparatus utilizing deflectable laser beams," U.S. patent 4,978,219 (18 December 1990).

11. C. J. R. Sheppard and H. Zhou, "Confocal interference microscopy," in *Three-Dimensional Microscopy: Image Acquisition and Processing IV,* C.J. Cogswell, J.A. Conchello, and T. Wilson, eds, Proc. SPIE **2984,** 85–89 (1997).

12. P. F. Meilan and M. Garavaglia, "Fizeau confocal laser scanning interference microscope," in *Selected Papers from International Conference on Optics and Optoelectronics '98,* K. Singh, O.P. Nijhawan, A.K. Gupta, and A. K. Musla, eds. Proc. SPIE **3729,** 384–389 (1999).

13. M. Davidson, K. Kaufman, I. Mazor, and F. Cohen, "An application of interference microscopy to integrated circuit inspection and metrology," in *Integrated Circuit Metrology, Inspection, and Process Control,* K. M. Monahan, ed., Proc. SPIE **775,** 233–247 (1987).

14. D. M. Gale, M. I. Pether, and J. C. Dainty, "Linnik microscope imaging of integrated circuit structures" Appl. Opt. **35,** 131–148 (1996).

15. G. S. Kino and S. S. C. Chim, "Mirau correlation microscope," Appl. Opt. **29,** 3775–3783 (1990).

16. P. J. Caber, "Interferometric profiler for rough surfaces," Appl. Opt. **32,** 3438–3441 (1993).

17. L. Deck and P. de Groot, "High-speed noncontact profiler based on scanning white-light interferometry," Appl. Opt. **33,** 7334–7338 (1994).

18. J. C. Wyant and K. Creath, "Advances in interferometric optical profiling," Int. J. Mach. Tools Manufact. **32,** 5–10 (1992).

19. P. de Groot and L. Deck, "Surface profiling by analysis of white-light interferograms in the spatial frequency domain," J. Mod. Opt. **42,** 389–401 (1995).

20. B. S. Lee and T. C. Strand, "Profilometry with a coherence scanning microscope," Appl. Opt. **29,** 3784–3788 (1990).

21. W. J. Tango, "Dispersion in stellar interferometry," Appl. Opt. **29,** 516–521 (1990).

22. P. R. Lawson and J. Davis, "Dispersion compensation in stellar interferometry," Appl. Opt. **35,** 612–620 (1996).

23. A. Pfortner and J. Schwider, "Dispersion error in white-light Linnik interferometers and its implications for evaluation procedures," Appl. Opt. **40,** 6223–6228 (2001).

24. P. de Groot, X. Colonna de Lega, J. Kramer, and M. Turzhitsky, "Determination of fringe order in white-light interference microscopy," Appl. Opt. **41,** 4571–4578 (2002).

25. J. J. Sniegowski and M. P. de Boer, "IC-compatible polysilicon surface micromachining," Annu. Rev. Mater. Sci. **30,** 299–333 (2000).

26. J. E. Greivenkamp and J. H. Bruning, "Phase shifting interferometry," in *Optical Shop Testing*, 2nd ed., D. Malacara, ed., (Wiley Interscience, 1992), pp. 501–598.

27. P. Hariharan, B. F. Oreb, and T. Eiju, "Digital phase-shifting interferometry: A simple error-compensating phase calculation algorithm," Appl. Opt. **26,** 2504–2506 (1987).